

# Oxygen-Redox Activity in Non-Lithium-Excess Tungsten-Doped LiNiO<sub>2</sub> Cathode

A.S. Menon<sup>1,2,\*§</sup>, B.J. Johnston<sup>1,2,§</sup>, S.G. Booth<sup>1,2,3,4</sup>, L. Zhang<sup>2,5</sup>, K. Kress<sup>2,3</sup>, B.E. Murdock<sup>5</sup>, G. Paez Fajardo<sup>1,2</sup>, N.N. Anthonisamy<sup>1,2,3,6</sup>, N. Tapia-Ruiz<sup>1,2,5,7</sup>, S. Agrestini<sup>1,8</sup>, M. Garcia-Fernandez<sup>8</sup>, K. Zhou<sup>8</sup>, P.K. Thakur<sup>8</sup>, T.L. Lee<sup>8</sup>, A.J. Nedoma<sup>1,2,9</sup>, S.A. Cussen<sup>1,2,†</sup>, and L.F.J. Piper<sup>1,2,‡</sup>

<sup>1</sup> WMG, University of Warwick, Coventry CV4 7AL, United Kingdom

<sup>2</sup> The Faraday Institution, Quad One, Harwell Campus, Didcot OX11 0RA, United Kingdom

<sup>3</sup> Department of Materials Science and Engineering, The University of Sheffield, Sheffield S1 3JD, United Kingdom

<sup>4</sup> Integrated Graphene Ltd, Euro House, Stirling FK8 2DJ, United Kingdom

<sup>5</sup> Department of Chemistry, Lancaster University, Lancaster LA1 4YB, United Kingdom

<sup>6</sup> Jaguar Land Rover Inc., Coventry CV3 4LF, United Kingdom

<sup>7</sup> Department of Chemistry, Molecular Sciences Research Hub, White City Campus, Imperial College London, London W12 0BZ, United Kingdom

<sup>8</sup> Diamond Light Source Ltd., Diamond House, Harwell Science and Innovation Campus, Didcot OX11 0DE, United Kingdom

<sup>9</sup> Department of Chemical and Biological Engineering, University of Sheffield, Sheffield S1 3JD, United Kingdom

(Received 21 October 2022; revised 7 February 2023; accepted 21 February 2023; published 13 March 2023)

The desire to increase the energy density of stoichiometric layered LiTMO<sub>2</sub> (TM = 3d transition metal) cathode materials has promoted investigation into their properties at high states of charge. Although there is increasing evidence for pronounced oxygen participation in the charge compensation mechanism, questions remain whether this is true O-redox, as observed in Li-excess cathodes. Through a high-resolution O K-edge resonant inelastic x-ray spectroscopy (RIXS) study of the Mn-free Ni-rich layered oxide LiNi<sub>0.98</sub>W<sub>0.02</sub>O<sub>2</sub>, we demonstrate that the same oxidized oxygen environment exists in both Li-excess and non-Li-excess systems. The observation of identical RIXS loss features in both classes of compounds is remarkable given the differences in their crystallographic structure and delithiation pathways. This lack of a specific structural motif reveals the importance of electron correlation in the charge compensation mechanism for these systems and indicates how a better description of charge compensation in layered oxides is required to understand anionic redox for energy storage.

DOI: 10.1103/PRXEnergy.2.013005

## I. INTRODUCTION

Interest in LiNiO<sub>2</sub> and its doped derivatives as future Li-ion battery (LIB) cathodes has been revived recently due to their ability to harness practical capacities close to the theoretical value [1–3]. To achieve high states of charge (SOCs) increasing the cell energy density,

cation plus anion redox is often necessary [4]. In practice, this often requires high-voltage operation to facilitate increased delithiation, which induces various degradation modes, namely, structural instabilities, parasitic electrode-electrolyte reactions, surface reconstructions, and oxygen loss, within the cathode that drastically reduce their cycle life [5–7]. To mitigate such processes, and therefore, maintain high energy densities over long-term cycling, we need to understand the structural and electronic changes in these cathodes at extreme states of delithiation and high voltages (>4.5 V vs Li/Li<sup>+</sup>) [1]. A key challenge here is to characterize the charge compensation mechanisms operating at these voltages. Recent O K-edge resonant inelastic x-ray spectroscopy (RIXS) investigations [8] into LiNiO<sub>2</sub> [9] cathodes and their doped variants [10] revealed that the capacity evolution did not follow a simple Ni<sup>3+</sup> to Ni<sup>4+</sup> oxidation step per unit delithiation (based on the ionic approximation) and that oxygen (i.e., O<sup>2-</sup>) was involved

\*ashok.menon@warwick.ac.uk

†S.Cussen@Sheffield.ac.uk

‡Louis.Piper@Warwick.ac.uk

§A. S. Menon and B. J. Johnston contributed equally to this work.

Published by the American Physical Society under the terms of the Creative Commons Attribution 4.0 International license. Further distribution of this work must maintain attribution to the author(s) and the published article's title, journal citation, and DOI.

in charge compensation towards the end of delithiation (at >4.5 V). Currently, it is not clear whether this is bona fide O-redox similar to that observed for Li-excess cathodes [11].

Oxygen redox in LIB cathodes was initially hypothesized and investigated for layered Li-excess compounds ( $\text{Li} : \text{TM} > 1$ ) due to their anomalous “excess” capacity during initial cycles that could not be explained solely using transition metal (TM) oxidation [12,13]. The excess capacity, attributed to  $\text{O}^{2-}$  oxidation, was argued to stem from nonbonding orphaned oxygen states formed as a result of  $\text{Li}-\text{O}-\text{Li}$  structural configurations [14]. Recent high-resolution RIXS (HR-RIXS) studies ascribed the ‘excess’ capacity during charging to  $\text{O}^{2-}$  oxidation within the bulk, resulting in trapped molecular  $\text{O}_2$  (while ruling out other  $\text{O}-\text{O}$  dimers, such as peroxide and superoxide) inside vacancy clusters formed through in-plane TM migration [15,16]. At the surface,  $\text{O}^{2-}$  oxidation leads to irreversible  $\text{O}_2$  loss. The bulk  $\text{O}^{2-} \rightarrow \text{O}_2$  oxidation phenomenon was also to other Li-excess [17,18] and Na intercalation cathodes [19,20]. Further corroboration was provided by small-angle x-ray scattering and neutron total scattering studies of charged Li-excess cathodes, which revealed nanoscale domains of lower electron density or nanopores and trapped  $\text{O}-\text{O}$  dimers with a bond length of about 1.2 Å in the cathode bulk, respectively [21,22]. However, alternate theories for the O-redox behavior do exist that do not require TM migration and nanopore formation [23], e.g., O-holes arising from the rehybridization of the TM–O orbital states during delithiation.

Unlike Li-excess cathodes, conventional layered stoichiometric (non-Li-excess;  $\text{Li} : \text{TM} = 1$ ) cathodes such as  $\text{LiCoO}_2$  and its derivatives do not show any capacity that cannot be accounted for by the TM redox couple [23]. Nevertheless, early investigations of their highly delithiated phases did lead to hypotheses of oxygen involvement in charge compensation [24–26]. Experimental proof for this was obtained only recently, with O-redox activity at high states of delithiation confirmed in several non-Li-excess cathodes, including  $\text{LiCoO}_2$  [27–29],  $\text{LiNiO}_2$  (and variants), [9,10,30]  $\text{LiNi}_{1/3}\text{Mn}_{1/3}\text{Co}_{1/3}\text{O}_2$  [31],  $\text{LiNi}_{0.6}\text{Mn}_{0.2}\text{Co}_{0.2}\text{O}_2$  [32],  $\text{LiNi}_{0.83}\text{Co}_{0.12}\text{Mn}_{0.05}\text{O}_2$  [33], and  $\text{LiNi}_{0.8}\text{Co}_{0.15}\text{Al}_{0.05}\text{O}_2$  [34]. Although charge compensation in these cathodes during (de)lithiation is considered to be solely due to TM-redox, these studies indicate that O-redox can occur after a certain state of delithiation. It is to be noted that conventional ionic approximations of cation and anion redox do not directly apply to these systems with significant covalent bonding and TM 3d and O 2p hybridization. In other words, it is difficult to demarcate the degree to which the TM and O species participate in charge compensation at specific stages of delithiation, and so, the charge compensation process may be better viewed as a joint process

involving both  $\text{TM}^{n+}$  and  $\text{O}^{n-}$  species. Therefore, understanding the O-redox behavior in such cathodes is a critical step in understanding how to harness O-redox-induced capacity enhancement.

It remains unclear whether Li-excess and stoichiometric cathodes have the same oxidized  $\text{O}^{2-}$  species because HR-RIXS has only thus far been applied to Li-excess cathodes. Most, if not all, O K-edge x-ray spectroscopy and RIXS studies on stoichiometric layered cathodes were performed on a high-efficiency RIXS beamline [35], which does not provide sufficient resolution to deconvolute the RIXS spectra to identify the vibronic structure of the oxidized  $\text{O}^{2-}$  species. In contrast, HR-RIXS sources provide the necessary resolution to do so. Nonetheless, bulk O-redox signatures observed using high-efficiency RIXS, namely, the emission feature at about 523.7 eV and the low-energy excitation near the elastic line at an excitation energy of about 531 eV, for both layered stoichiometric and Li-excess cathodes, in addition to certain Na analogues, are highly comparable [9,10,27,28,30–32,34,36–44]. This suggests a common origin for the O-redox behavior and that  $\text{Li}-\text{O}-\text{Li}$  configurations, which are generally absent in stoichiometric layered oxides and can only occur due to antisite disorder [2,45], may not be a prerequisite for O-redox. This warrants further investigation and identification of the nature of the oxidized  $\text{O}^{2-}$  species in stoichiometric layered cathodes is an important step.

To probe the nature of oxidized  $\text{O}^{2-}$  species in stoichiometric layered cathodes, we performed an O K-edge HR-RIXS study using 2%-tungsten-doped  $\text{LiNiO}_2$  ( $\text{LiNi}_{0.98}\text{W}_{0.02}\text{O}_2$ ) as a model system. In addition to its superior electrochemical performance compared to undoped  $\text{LiNiO}_2$  [46–49], it is a Mn-free system, which removed the possibility of theoretically predicted [50] but experimentally unverified  $\text{Mn}^{4+}$  to  $\text{Mn}^{7+}$  oxidation [37,51], and the stabilization of orphaned O 2p orbitals by Mn [52–54]. The crystallographic and electronic structure changes in the  $\text{LiNi}_{0.98}\text{W}_{0.02}\text{O}_2$  cathode as a function of delithiation were investigated using x-ray diffraction and spectroscopy methods. Oxygen participation in charge compensation was investigated through O K-edge soft x-ray absorption spectroscopy (XAS) and HR-RIXS. This combination enabled the joint probing of the O unoccupied and occupied valence states, thereby providing a clear picture of TM–O hybridization [8]. The HR-RIXS, in addition to detecting the presence of oxidized  $\text{O}^{n-}$  ( $n < 2$ ) species, also facilitated its identification [11]. Interestingly, the same HR-RIXS signature as that of charged Li-excess cathodes was seen here. Considering the differences in structural evolution during delithiation of these two cathode systems, it is possible that another explanation for the O-redox activity exists. This discovery also highlights the need to further understand the charge compensation

mechanisms in conventional stoichiometric layered cathodes at high states of charge.

## II. RESULTS AND DISCUSSION

### A. Pristine material and electrochemistry

$\text{LiNi}_{0.98}\text{W}_{0.02}\text{O}_2$ , referred to as WLNO, was synthesized through the high-temperature calcination of  $\text{LiOH}\cdot\text{H}_2\text{O}$ ,  $\text{WO}_3$ , and coprecipitated  $\text{Ni(OH)}_2$  (see Supplemental Material Sec. 1.1 [55]). The WLNO sample was polycrystalline in nature, with micron-sized agglomerates composed of primary particles [Fig. 1(a)]. Powder x-ray diffraction (XRD) data [Fig. 1(b)] of pristine WLNO could be fitted with a rhombohedral  $R\bar{3}m$  unit cell, with refined lattice parameters comparable to those in the literature (Table S1 within the Supplemental Material [55]) [46,48,49]. No traces of unreacted precursors were seen. However, there is compelling evidence that true bulk W doping (i.e., W occupying Li and/or Ni sites) does not occur in WLNO and that amorphous  $\text{Li}_x\text{W}_y\text{O}_z$  phases form along grain boundaries and particle surfaces [34,36].

This makes the bulk Li deficient, leading to the formation of off-stoichiometric phases. Evidence for amorphous  $\text{Li}_x\text{W}_y\text{O}_z$  phases could be seen in the XRD data [Fig. 1(b), inset] as the broad bump near the 003 reflection [36]. Nevertheless, the reported effects of W doping, such as increased lattice parameters and peak broadening, were clearly seen in the WLNO XRD data when compared to undoped  $\text{LiNiO}_2$  (Fig. S1 within the Supplemental Material [55]) [33,36].

Structural analysis of the pristine WLNO was done through Rietveld refinement [56,57] against XRD data (Supplemental Material Sect. 2.3 [55]).  $\text{LiNiO}_2$  often exists as off-stoichiometric Li-deficient  $\text{Li}_{1-z}\text{Ni}_{1+z}\text{O}_2$  ( $z < 1$ ) phases [2,58]. Excess Ni is present in the Li layer ( $3b$  site) as  $\text{Ni}^{2+}$ . Thus, an accurate structural representation of  $\text{LiNiO}_2$  would be  $[\text{Li}_{1-z}^+\text{Ni}_z^{2+}]_{3b}[\text{Ni}_z^{2+}\text{Ni}_{1-z}^{3+}]_{3a}[\text{O}_2^{2-}]_{6c}$ , where  $z < 1$  and the subscripts outside the parentheses denote the crystallographic ( $R\bar{3}m$ ) sites. Considering this complexity, Rietveld analysis was performed in two stages, with and without W in the bulk, to avoid overparameterizing the XRD data.  $\text{Li}_x\text{W}_y\text{O}_z$  phases were excluded in either case. First, the off-stoichiometry was

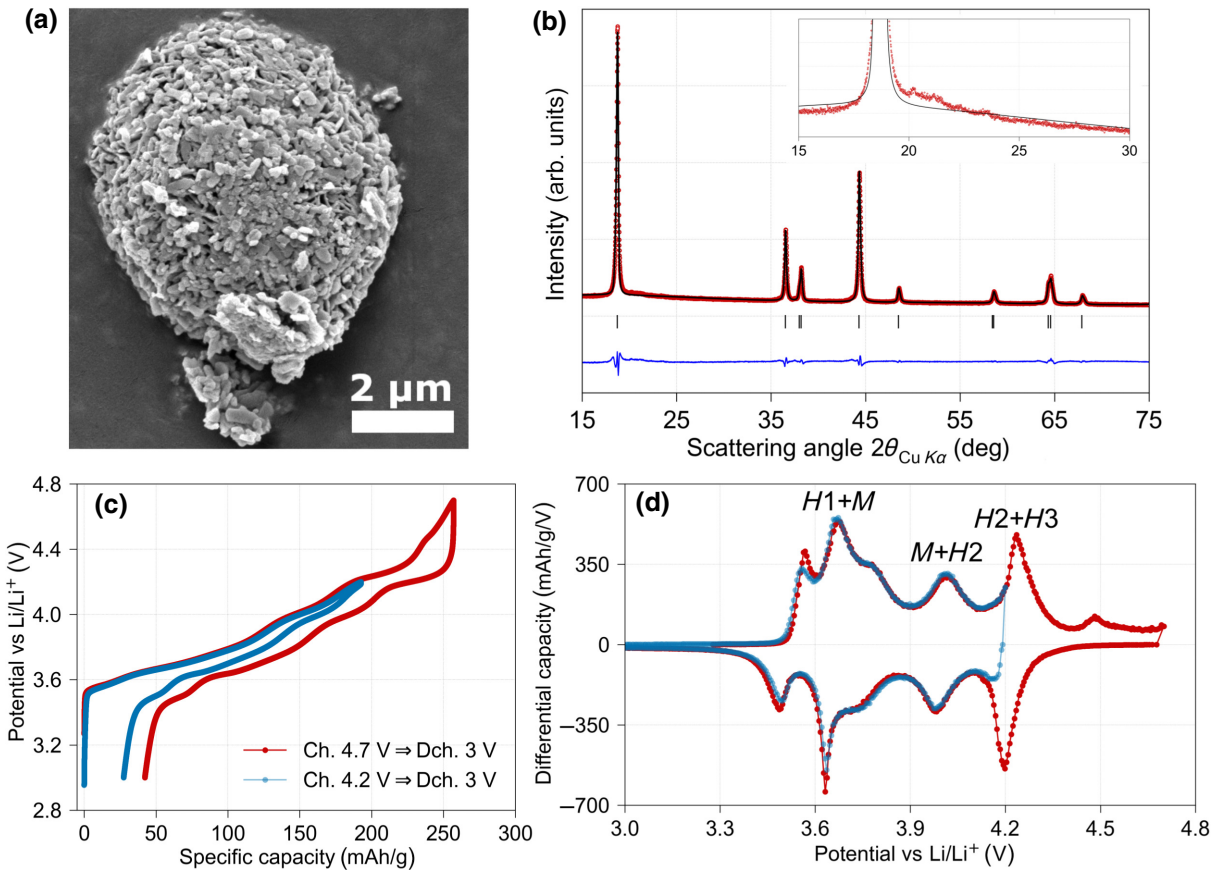


FIG. 1. (a) SEM image of a WLNO particle. (b) XRD data fitted with a  $R\bar{3}m$  unit cell. Inset shows a magnified view of data between  $15^\circ$  and  $30^\circ$  ( $2\theta$ ). (c) Potential versus specific capacity plots of WLNO when charged to 4.2 V (blue) and 4.7 V (red) followed by discharge to 3 V. (d) Corresponding differential capacity plots ( $dQ/dV$ ), with the bulk structural phases labeled.  $H$  and  $M$  stand for hexagonal and monoclinic, respectively.

evaluated using the methodology outlined by Rougier *et al.* [58], where the isotropic atomic displacement parameter of Li ( $B_{\text{Li}}$ ) was used as a qualitative indicator of the same. As expected, structural refinement of a  $\text{LiNiO}_2$  phase resulted in a  $B_{\text{Li}}$  value of  $-3.95(15) \text{ \AA}^2$ , due to excess electronic density from  $\text{Ni}^{2+}$  in the Li site. Repeating the same with 2% W on the Ni site led to comparable values of  $-4.09(15) \text{ \AA}^2$ . Second, refinements were performed to evaluate the degree of Li–Ni mixing, i.e., Ni on the Li (3b) site. Here, the site occupancy of the Li (3b) site with both Li and Ni was allowed to refine with the atomic displacement parameters held constant. For  $\text{LiNiO}_2$  without W, the Li site occupancy refined to include 2.29(18)% Ni. A comparable value of 2.01(19)% was obtained when W was included in the structure ( $\text{LiNi}_{0.98}\text{W}_{0.02}\text{O}_2$ ). These values were lower than those previously reported for comparable W-doped  $\text{LiNiO}_2$  samples (~5%) [33,36,59]. This is most likely a consequence of the solid-state doping approach, which can impart a higher degree of heterogeneity in W doping due to its inherently sluggish kinetics [42]. The refinements show that WLNO exhibited off-stoichiometry with an appreciable amount of Ni present in the Li layer and that W incorporation happens predominantly at the microstructural and surface levels. More importantly, this precludes the formation of Li–O–Li configurations in the material, which is relevant to the discussion of O-redox activity.

Previous studies of 2% W-doped  $\text{LiNiO}_2$  samples have reported dissimilar surface and bulk structures [46,48]. Similar behavior was also seen here, based on XAS data. Ni  $K$ -edge x-ray absorption near-edge structure (XANES) data (Fig. S6 within the Supplemental Material [55]) for WLNO shows that the average bulk oxidation state of Ni is approximately +3. However, stark differences are seen in the Ni  $L_3$ -edge soft XAS data, which can be qualitatively evaluated using the ratio of the high- and low-energy peaks in the edge [60]. Note that the soft XAS data were collected using the WLNO electrode in the open circuit voltage (OCV) state, whereas the Ni  $K$ -edge XANES data were measured using a pelletized powder sample. As shown in Fig. S7 within the Supplemental Material [55], the Ni soft XAS data collected in surface-sensitive electron yield (EY) mode and sub-surface-sensitive fluorescent yield (FY) mode, are noticeably different, indicating that the Ni oxidation state is not uniform within the sample. The EY data (<10 nm probing depth) conforms to a lower Ni oxidation state akin to  $\text{Ni}^{2+}$ , while the FY data (~100 nm probing depth) resembles a higher  $\text{Ni}^{3+}$  oxidation state [61]. The detection of  $\text{Ni}^{2+}$  at the surface suggests that a cation ordered structure might be formed at the surface, which aligns with previous studies [46,62].

The first cycle electrochemical data of WLNO (vs.  $\text{Li}/\text{Li}^+$ ) charged to 4.7 V and then discharged to 3 V, is shown in Fig. 1(c). Data corresponding to an upper cutoff

voltage of 4.2 V is also included for comparison. The theoretical capacity of WLNO, calculated using Ni oxidation alone, was ~262 mAh/g. When charged to 4.2 V, a capacity of about 192 mAh/g, corresponding to about 0.73 moles of delithiation, was obtained. Upon increasing the upper cutoff voltage to 4.7 V, the capacity increased to about 257 mAh/g, indicative of about 0.98 moles of delithiation. Therefore, no “excess” capacity that could not be accounted for by Ni oxidation was observed. When discharged, capacities of 165.2 and 214.8 mAh/g were obtained for cells charged to 4.2 and 4.7 V, respectively. Similar to undoped  $\text{LiNiO}_2$ , increasing the upper cutoff voltage from 4.2 V to 4.7 V also led to higher voltage hysteresis, as seen in Fig. 1(c) [46]. The differential capacity plot in Fig. 1(d) shows that the structural transitions previously reported for  $\text{LiNiO}_2$  and its derivatives, involving a monoclinic ( $M$ ) phase and different hexagonal ( $H$ ) phases, are present here as well [33,36,46]. Compared to similar samples from other studies [46,48], the redox peaks are more pronounced, indicating that the structural phase transitions were more abrupt. This is most likely due to the aforementioned differences in the degree of W doping as a consequence of the different synthetic protocols employed in the studies. Additionally, a small peak is seen at about 4.5 V during charging alone. This is attributed to interfacial electrode-electrolyte reactions during the first charge [9].

## B. Structural evolution during cycling

The structural evolution of WLNO during electrochemical cycling was characterized *ex situ* using XRD. Six conditions, namely, OCV, charged to 3.8 V (~0.4 mol delithiation), charged to 4.2 V (~0.73 mol delithiation), charged to 4.5 V (~0.92 mol delithiation), charged to 4.7 V (~0.96 mol delithiation), and discharged to 3 V after charging to 4.7 V, were studied. As seen in Fig. 2(a), charging to 4.2 V led to an expected bulk structure evolution [46,64]. The 003 reflection [Fig. 2(a), center panel], representative of the interlayer spacing, moves towards lower scattering angles as the layered structure expands because of the increased interlayer  $\text{O}^{2-}$ – $\text{O}^{2-}$  repulsion. Concurrently, a steep decrease in the  $a$  lattice parameter is observed due to decreasing Ni–O bond distance as a consequence of Ni oxidation. The hexagonal to monoclinic transformation ( $H1$  to  $M$ ) is not visible in the XRD data here, as it occurred between 3.8 and 4.2 V [46]. The refined  $R\bar{3}m$  unit cell values are provided in Table S6 (Supplemental Material Sec. 4 [55]). The  $H2$ – $H3$  transformation is understood to be complete by about 4.4 V, as per the differential capacity plot and previous studies [46,65]. Beyond 4.4 V (i.e., >0.7 moles of delithiation), the structural transformations became complex [66]. This is reflected in the poor quality of the Pawley fit of the 4.5 V and 4.7 V XRD data using a single  $R\bar{3}m$  unit cell. Due to this complexity and limited reciprocal space resolution of the laboratory

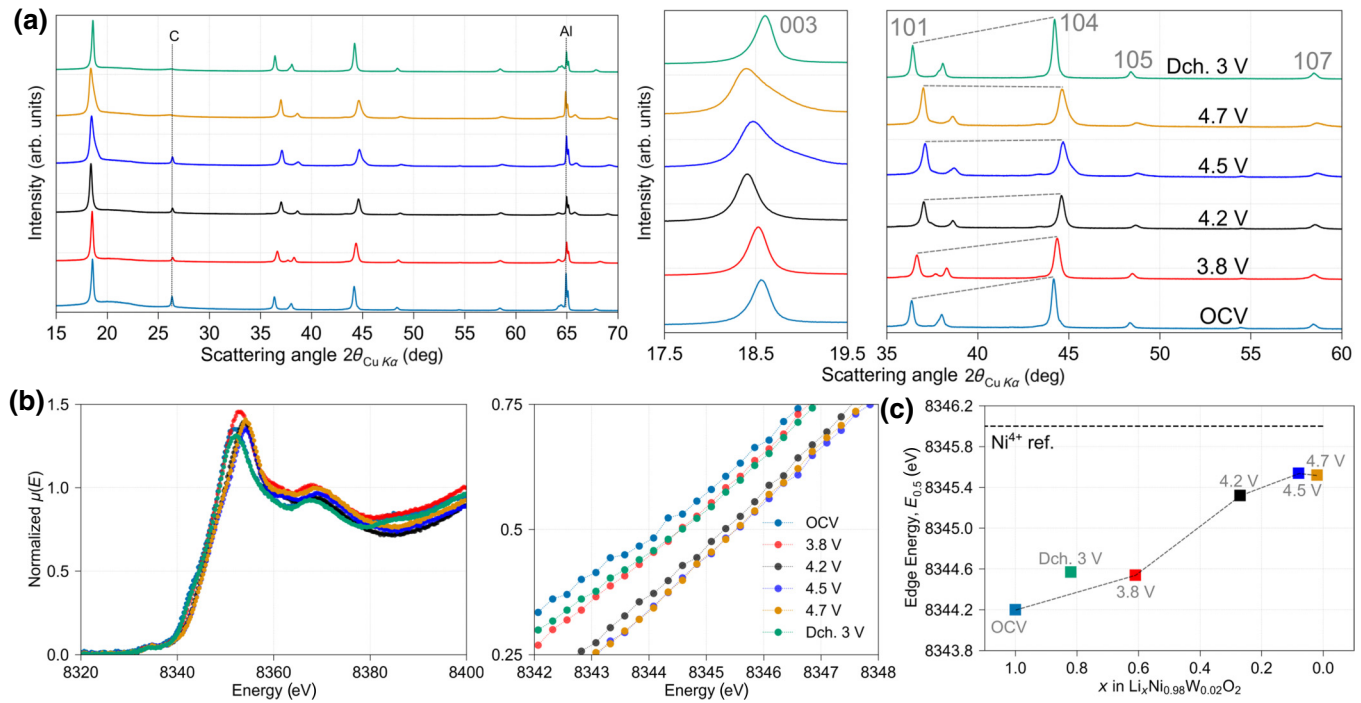


FIG. 2. (a) *Ex situ* XRD data of the WLNO electrodes stacked along  $y$ . Most intense peaks of C and Al from the electrodes are highlighted. Magnified views of different regions are shown in the center and right panels. Certain Bragg reflections ( $R\bar{3}m$ ) are highlighted. Legend in the right panel applies to the two panels to the left as well. (b) Corresponding XANES data from the electrodes, with a magnified view of the edge (center panel).  $\mu(E)$  is the absorption coefficient. (c) Ni  $K$ -edge energy shift as a function of Li content in WLNO. OCV and charged electrodes are linked with a line as a guide to the eye. “Dch.” refers to discharged.  $\text{Ni}^{4+}$  reference is  $\text{BaNiO}_3$  [63].

XRD data, only a qualitative analysis of highly delithiated WLNO structures is provided to avoid overinterpretation.

Previous investigations of highly delithiated  $\text{Li}_x\text{NiO}_2$  phases provide a good platform to understand the structural changes in the WLNO cathodes that were charged to 4.5 V and 4.7 V. Here, the cathodes have  $<0.1$  mol of Li in the bulk. At these stages, the O3-type oxygen layer stacking in the H3 phase began to transform into the O1-type (sometimes referred to as the H4 phase) [25,67] with the concomitant generation of stacking faults [25,30,67,68]. The nature, extent, and mechanism of this transformation are currently not well understood, due to differences in the pristine material properties, extent of delithiation, and charging protocols [66]. For example, the O3 to O1 transformation was reported to be suppressed or hindered in  $\text{LiNiO}_2$  until full delithiation based on *operando* XRD [69] and first-principles calculations [70]. However, there is ample evidence for the presence of O1-type stacking in highly delithiated  $\text{Li}_x\text{NiO}_2$  [30,71,72]. In WLNO, XRD data of the 4.5 V and 4.7 V cathodes are similar to each other, while being distinctly different from the rest. The 003 reflection was asymmetrically broadened towards higher scattering angles similar to those reported by Croguennec *et al.* [25,67] and ascribed to the coexistence of two phases, H3 (called R3 in their work) and

H4, with O3- and O1-type stacking [73], respectively. We posit that the same is true for the 4.5 V and 4.7 V WLNO cathodes as well. This is further corroborated by the significant asymmetric broadening of the 10 $\bar{l}$  and 01 $\bar{l}$  reflections [Fig. 2(a), right-most panel], which reveal the presence of stacking faults in the structure [25]. Another notable difference in the 4.5 V and 4.7 V charged samples is the increasing intensity of the 101 reflection with respect to the 104 reflection. This was previously linked to the migration of Ni from the TM layer to the tetrahedral sites in the Li layer, which suppresses the O3 to O1 transformation [69]. However, this is unlikely as significant broadening of the 10 $\bar{l}$  reflections (due to stacking faults) suggest that O1 stacking is present in the structure, which might lead to the same effect [25]. It is also unlikely that  $\text{Ni}^{4+}$  is stabilized in a tetrahedral site [74]. Recent studies have suggested that Li-Ni interlayer mixing occurs in Ni-rich layered cathodes at high states of charge, based on an increase in the intensity of the 104 reflection [30,33]. This was not seen here, indicating that the Li-Ni interlayer mixing is not significant in the case of WLNO. It remains to be seen whether W doping has a direct impact on this. Upon discharging to 3 V, the original layered structure was regained, indicating that the bulk structural evolution during charging is, on average, reversible.

### C. Evolution of bulk Ni oxidation states

The extent of bulk Ni oxidation in the WLNO cathodes was investigated using Ni *K*-edge XANES (in transmission). Previous XAS investigations have shown that the bulk Ni oxidation in LiNiO<sub>2</sub> cathodes increases steadily during charging and reaches approximately +4 upon near-complete delithiation [25,75]. However, there is also evidence that Ni oxidation does not increase continuously during charging in Ni-rich layered cathodes, and instead plateaus towards the end of charging [9,34]. For WLNO, as seen in Fig. 2(b), the bulk Ni oxidation increased during charging until 4.5 V, reaching very close to the formal Ni<sup>4+</sup> state, based on BaNiO<sub>3</sub> [63]. This is clearly seen in the evolution of the Ni edge position [half-height of normalized spectra, Fig. 2(c)]. Upon discharging to 3 V, Ni reduced to a state close to that in the OCV cathode. Expectedly, it was not totally reversible due to the associated voltage hysteresis (and capacity loss) shown in Fig. 1(c). Of note was that the Ni oxidation state dramatically slowed down upon charging to 4.7 V from 4.5 V (~0.06-mole delithiation), and no notable changes in Ni XANES are seen. This can be interpreted as an indication of O participation in charge compensation. However, it must be noted that the analyses of the Ni *K*-edge position using the half-height method, while convenient, is prone to analytical error due to possible changes in the line shape of the absorption edge. Having characterized the bulk crystallographic and electronic structure of WLNO, a detailed study of the surface and bulk oxygen environment, focusing on the three cathodes at the charge and discharge limits, i.e., OCV, charged to 4.7 V, and discharged to 3 V, is presented.

### D. Evolution of surface species

The evolution of the surface structure was characterized using the O *K*-edge and Ni *L*<sub>3</sub>-edge soft XAS data collected in EY mode. As seen in Fig. S9 within the Supplemental Material [55], the data revealed a reversible behavior during the first cycle. The peak at about 534 eV in the O *K*-edge spectra indicates that a surface layer of Li<sub>2</sub>CO<sub>3</sub> was present on the OCV electrode [76], which was completely removed upon charging, only to be formed again on discharging. The different Ni oxidation states in the surface and subsurface in the FY [Fig. 2(b)] and EY (Fig. S10 within the Supplemental Material [55]) data show that the extent of Ni oxidation upon charging was not uniform across the cathode. Ni was oxidized to a much higher degree in the subsurface and reached oxidation states close to +4, which is in good agreement with the Ni *K*-edge XANES data presented here and previously in the literature [77]. The hard x-ray photoelectron spectroscopy data collected at two different incident photon energies for greater sampling depth shows that true bulk delithiation occurred at the surface and subsurface or bulk regions. This was seen in Fig. S11 within the Supplemental Material [55],

where the charged cathode data does not include any peaks in the Li 1s core-level binding energy region. Furthermore, the shift in the Ni core-level (*2p* and *3p*) reveals that simultaneous oxidation of Ni also happened during delithiation. The presence of Li-W-O species on the particle surface will affect the cathode-electrolyte interphase and complicates a comprehensive analysis. Nonetheless, the surface analysis data presented indicates that O<sup>2-</sup> oxidation happens in the bulk and, by extension, O-redox activity occurs at high states of charge in the WLNO cathode.

### E. Bulk O-redox

The bulk O-redox activity in WLNO cathodes was investigated through O *K*-edge soft XAS and HR-RIXS. The soft XAS spectra and RIXS line scans are shown in Figs. 3(a) and 3(b), respectively. Additionally, all of the HR-RIXS maps and the line scan data are shown in Supplemental Material Sec. 7 [55]. As highlighted in the soft XAS spectra [Fig. 3(a)], charging WLNO to 4.7 V led to the formation of additional O unoccupied states at about 531 eV, which was similar to LiNiO<sub>2</sub> and Li-excess systems [9,15]. In the corresponding RIXS scan of the charged sample collected at this incident energy (531 eV), a new energy-loss feature, namely, a series of peaks corresponding to a vibronic structure is observed close to the elastic peak (0 eV). This is absent in the OCV and discharged cathode spectra. The peak spacing of the energy-loss feature of the WLNO 4.7 V charged sample is highly comparable, if not identical, to that previously reported for all charged Li-excess and certain layered Na cathode materials [15–20]. Note that extremely weak energy-loss features are visible in averaged RIXS data for the OCV and discharged cathodes, possibly due to the various cathode-electrolyte interphase species formed, as shown in Fig. S15 in the Supplemental Material [55], but the peak spacing of these weak features does not match those of the charged sample.

In Fig. 3(c), the dependence of the peak spacing on energy loss in the charged WLNO cathode was compared to that of the Li-excess cathode (Li<sub>1.2</sub>Mn<sub>0.54</sub>Ni<sub>0.13</sub>Co<sub>0.13</sub>O<sub>2</sub>) charged to 4.8 V from Ref. [15]. It is evident that the same linear decrease was seen in both cases, within error. This HR-RIXS feature has been used to confirm the presence of trapped molecular O<sub>2</sub> in the bulk of charged Li<sub>1.2</sub>Mn<sub>0.54</sub>Ni<sub>0.13</sub>Co<sub>0.13</sub>O<sub>2</sub> (and in cathodes similarly investigated through HR-RIXS). The peak separation of the lowest (first) energy-loss peak in WLNO and Li<sub>1.2</sub>Mn<sub>0.54</sub>Ni<sub>0.13</sub>Co<sub>0.13</sub>O<sub>2</sub>, i.e., the fundamental vibration frequency, was found to be about 0.19 eV, which corresponds to about 1550 cm<sup>-1</sup>. This is comparable to the value reported for molecular O<sub>2</sub> (~1556 cm<sup>-1</sup>) [78]. An additional energy-loss feature at about 7.5 eV (i.e., ~523.5 eV emission energy) was also seen in the WLNO RIXS scan, similar to trapped molecular O<sub>2</sub> and Li<sub>1.2</sub>Mn<sub>0.54</sub>Ni<sub>0.13</sub>Co<sub>0.13</sub>O<sub>2</sub>. This feature was previously

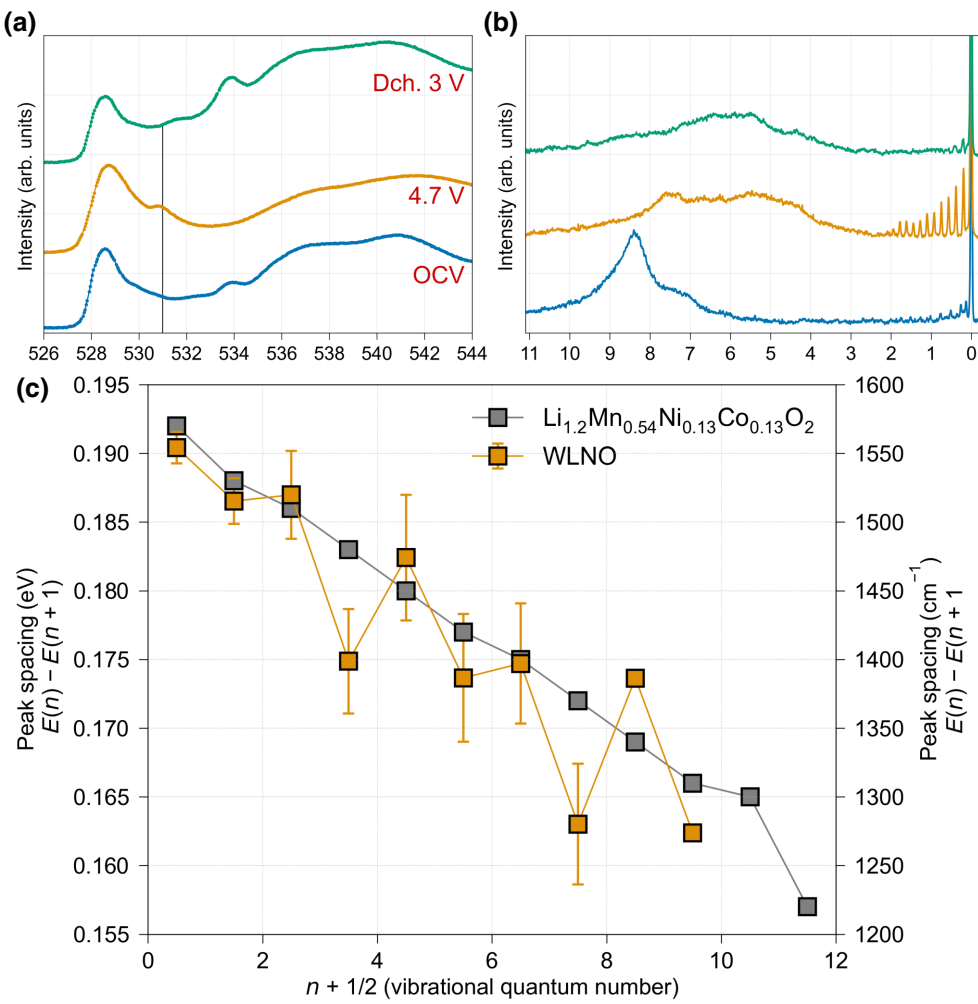


FIG. 3. (a) O  $K$ -edge spectra of WLNO collected in FY mode. Feature at about 531 eV is highlighted using a gray vertical line. (b) High-resolution O  $K$ -edge RIXS line scan collected at 531 eV. Only the OCV, charged to 4.7 V, and discharged to 3 V samples were measured. Legend from (a) is also applicable to (b). (c) Plot showing the linearly decreasing dependence of peak spacing for charged WLNO (4.7 V) and  $\text{Li}_{1.2}\text{Mn}_{0.54}\text{Ni}_{0.13}\text{Co}_{0.13}\text{O}_2$  (4.8 V) from Ref. [15] with respect to the vibrational quantum number,  $n$ . Each data point is an average from 15 scans.

assigned to the occupied  $\pi$  molecular orbitals on  $\text{O}_2$  [18]. Based on this, it could be assumed that molecular  $\text{O}_2$  is formed in the bulk of WLNO charged to 4.7 V, and the origin of the RIXS feature should be the same as that reported in  $\text{Li}_{1.2}\text{Mn}_{0.54}\text{Ni}_{0.13}\text{Co}_{0.13}\text{O}_2$  and other charged O-redox cathodes [15–20]. However, rationalizing the formation of trapped bulk molecular  $\text{O}_2$  in the non-Li-excess WLNO cathode using the same reasoning as that in Li-excess cathodes is not straightforward.

#### F. O-Redox behavior in non-Li-excess cathode materials

Multiple theories have been proposed to explain O-redox in LIB cathodes, but a universal one directly applicable to both Li-excess and layered stoichiometric cathodes does not yet exist [11,23,79–81]. The bulk

$\text{O}^{2-} \rightarrow (\text{trapped}) \text{O}_2$  oxidation theory of Li-excess systems cannot be directly extended to stoichiometric systems due to the crystallographic differences between the two. Layered Li-excess systems like  $\text{Li}_{1.2}\text{Mn}_{0.54}\text{Ni}_{0.13}\text{Co}_{0.13}\text{O}_2$  contain Li in the TM layer (0.2 mol in this case) and possess in-plane Li-TM ordering, unlike their layered stoichiometric counterparts [77,82]. Molecular  $\text{O}_2$  formed upon charging Li-excess cathodes is argued to be trapped within TM-layer vacancy clusters (nanopores) formed by simultaneous delithiation and in-plane TM migration [11]. Therefore, the presence of Li in the TM layers and in-plane Li-TM ordering is key to facilitating bulk molecular  $\text{O}_2$  formation. In other words, the formation and dissociation of the  $\text{O}_2$  dimer is considered to be the charge compensation mechanism for O-redox. Given that WLNO shows HR-RIXS features identical to Li-excess systems, either  $\text{O}_2$  dimer formation in nanopores is contributing to its

charge compensation or another mechanism needs to be considered for both systems.

In stoichiometric layered oxides, Li content in the TM layer is significantly lower than Li-excess compounds and is dependent on the paired antisite disorder (inter-layer Li-Ni mixing). It is generally reported to be <6% and decreases with increasing Ni content [83,84]. In compounds with >95 at. % Ni, Li is in fact absent from the TM layers due to off-stoichiometry [58]. Consequently, neither is there long-range Li-TM ordering [82,85] nor is there significant bulk TM migration during the delithiation of Ni-rich stoichiometric layered cathodes [37,84,86]. Thus, the concentration of Li–O–Li configurations and proclivity for delithiation-induced TM migration and vacancy clustering is significantly reduced, if not absent, in stoichiometric layered cathodes. In other words, there is minimal evidence for nonbonding orphaned O states in the pristine material and for vacancy cluster and nanopore formation needed to trap molecular O<sub>2</sub>. This was corroborated using small-angle x-ray scattering where no vacancy clusters were observed in charged LiNi<sub>0.8</sub>Co<sub>0.15</sub>Al<sub>0.05</sub>O<sub>2</sub> and LiNi<sub>0.4</sub>Mn<sub>0.4</sub>Co<sub>0.2</sub>O<sub>2</sub> [22]. Furthermore, O-redox behavior has been reported for LiNi<sub>0.8</sub>Co<sub>0.15</sub>Al<sub>0.05</sub>O<sub>2</sub>, which suggests that vacancy clustering is not necessary for O-redox [34]. As a result, the observation of identical HR-RIXS features does not support O<sub>2</sub> dimerization and dissociation as a universal charge compensation mechanism and other theories must be reconsidered. A recent density-functional theory (DFT) plus dynamic mean-field theory (DMFT) study reexamined the rehybridization mechanism associated with delithiation with Li<sub>x</sub>NiO<sub>2</sub> and concluded that the classical view of an ionic fixed O<sup>2-</sup> oxidation state is not valid; instead, there is significant oxygen participation, resulting in oxygen hole formation. These calculations were supported by spectral simulations of Ni and O K-edge XAS [59]. Moreover, the study also demonstrated that the 531 eV O K-edge XAS and RIXS feature could originate from O-redox-induced water intercalation and O<sub>2</sub> dimer formation with lattice oxygen at high states of charge. As a result, the RIXS signature might not be a direct probe of the bulk O-redox mechanism, and further studies are required.

Currently, O K-edge XAS and RIXS is the *de facto* probe for investigating O-redox behavior in battery cathodes [8,80]. However, a direct correlation between the XAS or RIXS data and bulk O-redox activity requires more scrutiny. First, Li<sub>2</sub>MnO<sub>3</sub>, historically touted as bulk O-redox active, has failed to show any O-redox signatures in O K-edge XAS studies [87]. Second, the aforementioned O K-edge emission feature was not observed in Li<sub>3</sub>IrO<sub>4</sub>, wherein delithiation is compensated solely by bulk O<sup>2-</sup> oxidation involving the generation of lone pairs [88]. Finally, as mentioned before, all O-redox-active charged stoichiometric layered, Li-excess, and certain Na cathodes studied using RIXS thus far, despite the differences in their pristine structure and delithiation pathways, show the same

~523.7 eV emission feature and low-energy excitations close to the elastic line (i.e., asymmetric broadening) at an excitation energy of 531 eV during high-efficiency RIXS mapping to varying degrees, irrespective of the composition and cycling protocol [9,10,27,28,30–32,34,36–44]. Therefore, it is only rational that the same HR-RIXS feature is also seen in both stoichiometric layered and Li-excess cathode systems.

Our results demonstrate the limitations of the terms “Ni” and “O” redox, based on simple ionic approximations to describe the delithiation of LiNiO<sub>2</sub>, and support the oxygen hole formation theory described in Ref. [59]. Further support come from recent *operando* neutron diffraction studies of Ni-rich cathodes [84,89], which reported an anomalous increase in the Ni–O bond length at extreme states of delithiation. This could be a direct consequence of bulk O<sup>2-</sup> oxidation that, when compared to previous reports, such as Refs. [90,91], points towards the involvement of electron hole states on the ligand (oxygen) 2p orbitals. Thus, the evolution of the electronic structure of layered stoichiometric and Li-excess oxide cathodes needs more consideration and direct experimental spectral validation. This is because conventional DFT methods fall short in calculating the electronic structure of these alkali transition-metal oxides due to their inability to account for electron correlation effects associated with TM 3d orbitals. For example, even for “simple” systems like NiO [92], Li-doped NiO [93], and LiCoO<sub>2</sub> [94], the presence of strong intraorbital coulomb interactions can lead to massive changes from expected band-theory behavior, with the presence of a ligand hole playing an important role in determining the electronic structure properties of the compounds. Modeling the electronic structure changes in such correlated systems is not trivial, as elaborated recently [95]. The framework of strongly correlated oxides was also suggested for Li-excess oxide cathodes [96]. Our work further supports the need for further beyond-DFT studies of layered oxides with experimental validation, such as Ref. [59], to better understand anionic redox chemistry of Li-excess systems.

### III. CONCLUSIONS

Intercalation-based energy storage systems centered on alkali transition-metal oxide redox requires understanding of the changes in their electronic and crystallographic structure associated with the changes in (electro)chemistry. In this study, we highlight how the concepts of TM- and O-redox need to be reexamined in “known” systems like Li<sub>x</sub>NiO<sub>2</sub>, i.e., does TM-O rehybridization facilitate oxygen redox? Using HR-RIXS, we demonstrate that the feature ascribed to trapped molecular O<sub>2</sub> in charged Li-excess cathodes is also seen in a stoichiometric Mn-free layered LiNi<sub>0.98</sub>W<sub>0.02</sub>O<sub>2</sub> cathode charged to 4.7 V, which does not show any capacity that could not be accounted for by

TM-redox. Neither does this material have Li–O–Li configurations in its pristine structure nor were there any clear indication of significant Ni migration upon delithiation required for nanopore formation compared to Li-excess systems. XRD analysis reveals that the structure of highly delithiated WLNO is a composite of O<sub>3</sub>- and O<sub>1</sub>-stacked phases. Ni *K*-edge XANES indicates formal Ni oxidation clearly ceased to reach +4 before full delithiation. The lack of a specific structural arrangement in Li-excess and stoichiometric layered cathodes and the strong possibility of TM-O rehybridization highlights the need for detailed computational studies beyond DFT-based methods. For example, Ref. [59] using DMFT and DFT demonstrated how O hole formation could facilitate charge compensation in LiNiO<sub>2</sub> at high states of delithiation supporting the X-ray spectroscopy data presented here. Electron correlation should explicitly be included in developing the theoretical descriptions of oxygen redox. It is hoped that this work will inspire further dedicated efforts within this field, which has the potential to help unlock design rules for stable oxygen redox in new cathode materials for energy storage applications.

## IV. EXPERIMENTAL DETAILS

### A. Synthesis of WLNO

The Ni(OH)<sub>2</sub> precursor was prepared via a precipitation method carried out in a stirred tank reactor (Eppendorf). Herein, the NiSO<sub>4</sub> solution (2 M, 162 ml) was pumped into a NH<sub>4</sub>OH solution (0.4 M, 598 ml) within the reactor. At the same time, a 2 M NaOH solution (NaOH : TM ratio = 2.0) and a NH<sub>4</sub>OH chelating agent solution (NH<sub>4</sub>OH : TM ratio = 1.2) were pumped separately into the reactor. The reaction was stirred overnight (1000 rpm, 20 h) and the Ni(OH)<sub>2</sub> precipitate was obtained after washing. The powder was dried at 80 °C overnight. The obtained Ni(OH)<sub>2</sub> powder was thoroughly mixed with LiOH·H<sub>2</sub>O and WO<sub>3</sub> powders (Li : Ni : W = 1.03 : 0.98 : 0.02 molar ratio) through hand-grinding. The mixture was transferred to a tube furnace and heated at 500 °C for 5 h followed by a final calcination at 750 °C for 15 h under a flow of oxygen.

### B. Electrochemistry

For electrochemical tests, the WLNO powder was mixed with C65 carbon black (Imerys) and polyvinylidene fluoride in a weight ratio of 95 : 5 : 5 in N-methyl-2-pyrrolidone (NMP) solvent. The obtained slurry was cast onto carbon-coated Al foil using a doctor blade set at a height of 150 µm. The slurry was dried at 100 °C to evaporate the NMP solvent before further drying at 80 °C overnight in a vacuum oven. Electrodes of 10 mm in diameter were then punched from the dried film and transferred into an Ar-filled glovebox.

CR2032 coin-type half-cells were constructed in an Ar-filled glovebox using the as-prepared WLNO electrodes as the cathode, a Li metal anode, and Whatman glass microfiber separator (plus an additional Celgard 2400 separator on the cathode side for cells that required post-cycling analysis). 1 M LiPF<sub>6</sub> in a mixture of ethylene carbonate (EC) and ethyl methyl carbonate (EMC) (EC : EMC 3 : 7 by wt %) with 2% vinylene carbonate additive (Solvionic) was used as the electrolyte. Galvanostatic charge and discharge tests were carried out to set voltages on an Arbin LBT21084 cycler at C/20 cycling rate (1 C = 220 mA g<sup>-1</sup>).

Cycled electrodes were collected from disassembled cells and washed with dimethyl carbonate (DMC) several times to remove any soluble surface species for *ex situ* measurements. Cell disassembly, electrode washing, and sample transfer took place in an Ar-filled glovebox.

### C. SEM

SEM images were collected on an FEI Inspect F50 instrument using an accelerating voltage of 5 kV. The powder sample was adhered to a carbon tab and gold coated using a sputter coater prior to inspection.

### D. XRD

XRD measurements of the pristine powders and cycled electrodes were carried out using a Malvern Panalytical Aeris diffractometer (40 kV, 15 mA) with nonmonochromated Cu *K*α radiation. On the incident beam side, a Ni Cu *K*β filter, a Soller slit (0.04 rad), a divergence slit (1/4°), and a 13-mm x-ray mask were used. Antiscatter (9 mm) and Soller (0.04 rad) slits were used on the diffracted beam side. Data from pristine powders were collected in Bragg-Brentano mode using a zero-background Si holder while spinning between an angular range of 10° and 75° (2θ) with a step size of about 0.01° and time per step of about 150 s, using a PIXcel1D-Medipix3 detector. Cycled electrodes retrieved from coin cells were measured *ex situ* under the same operating conditions using the same holder but with a Kapton film over it to prevent air exposure. The samples were prepared in an Ar-filled glove box. Pawley [97] and Rietveld [56,57] refinement analyses using the XRD data were performed using TOPAS-Academic (v7) software [98]. The refinement methodology was provided together with the results in appropriate sections.

### E. Ni *K*-edge XANES

XANES data of the pristine powders and cycled electrodes were collected using an easyXAFS300+ spectrometer [99]. The measurement was performed in transmission mode, with the Ni *K*-edge energy range accessed using a Si 551 spherically bent crystal analyzer. A helium gas chamber was used in the x-ray flight path to reduce air scattering. Measurements were made in the pre-edge and

XANES region with a step size of 0.25 eV and with 0.5 eV in the post-edge region. For powders, about 10 mg of the powder was pressed into pellets using cellulose (1 : 2 weight ratio), which were then held between Kapton tapes. The electrodes were sealed in 0.5 mm thick Kapton pouches inside an Ar-filled glovebox prior to measurement to prevent air exposure. Raw data were dead-time corrected, normalized (using the empty beam), and energy calibrated (using metallic Ni foil) with the instrument software. The subsequent pre-edge background subtraction and post-edge normalization were carried out using Athena software [100].

### F. XAS and RIXS

Soft XAS and HR-RIXS data were collected on the I21 beamline [101] at the Diamond Light Source, Oxford, UK. Measurements were carried out on electrodes recovered from coin cells and loaded onto the sample measurement pucks, which were transferred to the spectrometer under vacuum. Data were collected at 20 K under ultrahigh vacuum conditions, with continuous beam rastering. The incident x-ray energy was calibrated relative to the previously reported TM( $3d$ )-O( $2p$ ) peak of the LiNiO<sub>2</sub> O  $K$ -edge spectra [77]. Soft XAS data were obtained in total fluorescence and electron yield modes at the Ni  $L$  and O  $K$  edges with a step size of about 0.05 eV. The O  $K$ -edge soft XAS data were processed (pre-edge background subtraction and post-edge normalization) using Athena [100]. For the Ni  $L$ -edge data, background subtraction was carried out using the peak analyzer tool in OriginPro 2022. The baseline was created by the interpolation of manually selected background points. In all cases, the soft XAS data presented was an average of multiple individual scans.

For the O  $K$ -edge RIXS measurements, energy maps were collected between excitation energies of 526 eV and 536 eV with incremental steps of 0.25 eV. Following this, RIXS line scans for longer duration were performed at about 531 eV, chosen based on features observed in the RIXS maps. Carbon tape was measured for every RIXS spectrum collected to calibrate the elastic peak (0 eV) position. Processing of the raw data was performed using DAWN software [102] following the established procedure at the beamline. Spacing of the energy-loss features in the RIXS line scans was obtained by fitting Gaussian peaks to the data after background subtraction using OriginPro 2022.

### G. Hard x-ray photoelectron spectroscopy (HAXPES)

HAXPES measurements were performed at the I09 beamline, Diamond Light Source. As with the XAS and RIXS measurements, cycled electrodes were disassembled in the glovebox and rinsed with DMC before being loaded onto the sample puck. The pucks were then transferred to the measurement chamber without exposure to air, which

was then pumped to ultrahigh vacuum conditions over multiple days. Spectra were acquired using incident x-ray energies of 2.2 eV and 6.6 keV, to probe different electrode depths. Spectra were always collected on the same spot and sample damage upon prolonged x-ray exposure was checked by acquiring F 1s spectra after measurement of each sample. Energy calibrations were performed by setting the hydrocarbon peak to 285.0 eV.

### ACKNOWLEDGMENTS

The authors wish to acknowledge funding from the Faraday Institution for the Next Generation Lithium-Ion Battery projects FutureCat (FIRG017) and Degradation (FIRG024). We acknowledge Diamond Light Source for time on beamlines I21 and I09 under Proposals No. MM29104 and No. SI29113, respectively. The contributions from Dr. Xabier Martinez De Irujo Labalde and Professor Michael Hayward (University of Oxford) are gratefully acknowledged. Dr. Annalena R. Genreith-Schriever (University of Cambridge) is also acknowledged for their input. We are also grateful to the referees for their constructive reviews that have improved this work.

- [1] S. G. Booth, *et al.*, Perspectives for next generation lithium-ion battery cathode materials, *APL Mater.* **9**, 109201 (2021).
- [2] M. Bianchini, M. Roca-Ayats, P. Hartmann, T. Brezesinski, and J. Janek, There and back again—the journey of LiNiO<sub>2</sub> as a cathode active material, *Angew. Chem., Int. Ed.* **58**, 10434 (2019).
- [3] M. D. Radin, S. Hy, M. Sina, C. Fang, H. Liu, J. Vinckeviciute, M. Zhang, M. S. Whittingham, Y. S. Meng, and A. Van der Ven, Narrowing the gap between theoretical and practical capacities in Li-ion layered oxide cathode materials, *Adv. Energy Mater.* **7**, 1602888 (2017).
- [4] G.-H. Lee, V. W.-h. Lau, W. Yang, and Y.-M. Kang, Utilizing oxygen redox in layered cathode materials from multiscale perspective, *Adv. Energy Mater.* **11**, 2003227 (2021).
- [5] M. Jiang, D. L. Danilov, R.-A. Eichel, and P. H. L. Notten, A review of degradation mechanisms and recent achievements for Ni-rich cathode-based Li-ion batteries, *Adv. Energy Mater.* **11**, 2103005 (2021).
- [6] H. Zhang, H. Liu, L. F. J. Piper, M. S. Whittingham, and G. Zhou, Oxygen loss in layered oxide cathodes for Li-ion batteries: Mechanisms, effects, and mitigation, *Chem. Rev.* **122**, 5641 (2022).
- [7] C. S. Yoon, D.-W. Jun, S.-T. Myung, and Y.-K. Sun, Structural stability of LiNiO<sub>2</sub> cycled above 4.2 V, *ACS Energy Lett.* **2**, 1150 (2017).
- [8] W. Yang and T. P. Devvereaux, Anionic and cationic redox and interfaces in batteries: Advances from soft x-ray absorption spectroscopy to resonant inelastic scattering, *J. Power Sources* **389**, 188 (2018).

- [9] N. Li, S. Sallis, J. K. Papp, J. Wei, B. D. McCloskey, W. Yang, and W. Tong, Unraveling the cationic and anionic redox reactions in a conventional layered oxide cathode, *ACS Energy Lett.* **4**, 2836 (2019).
- [10] N. Li, S. Sallis, J. K. Papp, B. D. McCloskey, W. Yang, and W. Tong, Correlating the phase evolution and anionic redox in Co-free Ni-rich layered oxide cathodes, *Nano Energy* **78**, 105365 (2020).
- [11] R. A. House, J.-J. Marie, M. A. Pérez-Osorio, G. J. Rees, E. Boivin, and P. G. Bruce, The role of O<sub>2</sub> in O-redox cathodes for Li-ion batteries, *Nat. Energy* **6**, 781 (2021).
- [12] Z. Lu and J. R. Dahn, Understanding the anomalous capacity of Li/Li[Ni<sub>x</sub>Li<sub>(1/3-2x/3)</sub>]Mn<sub>(2/3-x/3)</sub>O<sub>2</sub> cells using *in situ* x-ray diffraction and electrochemical studies, *J. Electrochem. Soc.* **149**, A815 (2002).
- [13] C. S. Johnson, J. S. Kim, C. Lefief, N. Li, J. T. Vaughney, and M. M. Thackeray, The significance of the Li<sub>2</sub>MnO<sub>3</sub> component in ‘composite’ xLi<sub>2</sub>MnO<sub>3(1-x)</sub>LiMn<sub>0.5</sub>Ni<sub>0.5</sub>O<sub>2</sub> electrodes, *Electrochem. Commun.* **6**, 1085 (2004).
- [14] D. H. Seo, J. Lee, A. Urban, R. Malik, S. Kang, and G. Ceder, The structural and chemical origin of the oxygen redox activity in layered and cation-disordered Li-excess cathode materials, *Nat. Chem.* **8**, 692 (2016).
- [15] R. A. House, G. J. Rees, M. A. Pérez-Osorio, J.-J. Marie, E. Boivin, A. W. Robertson, A. Nag, M. Garcia-Fernandez, K.-J. Zhou, and P. G. Bruce, First-cycle voltage hysteresis in Li-rich 3d cathodes associated with molecular O<sub>2</sub> trapped in the bulk, *Nat. Energy* **5**, 777 (2020).
- [16] Q. Li, D. Ning, D. Wong, K. An, Y. Tang, D. Zhou, G. Schuck, Z. Chen, N. Zhang, and X. Liu, Improving the oxygen redox reversibility of Li-rich battery cathode materials via coulombic repulsive interactions strategy, *Nat. Commun.* **13**, 1123 (2022).
- [17] R. A. House, J.-J. Marie, J. Park, G. J. Rees, S. Agrestini, A. Nag, M. Garcia-Fernandez, K.-J. Zhou, and P. G. Bruce, Covalency does not suppress O<sub>2</sub> formation in 4d and 5d Li-rich O-redox cathodes, *Nat. Commun.* **12**, 2975 (2021).
- [18] R. Sharpe, R. A. House, M. J. Clarke, D. Forstermann, J. J. Marie, G. Cibin, K. J. Zhou, H. Y. Playford, P. G. Bruce, and M. S. Islam, Redox chemistry and the role of trapped molecular O<sub>2</sub> in Li-rich disordered rocksalt oxyfluoride cathodes, *J. Am. Chem. Soc.* **142**, 21799 (2020).
- [19] R. A. House, U. Maitra, M. A. Perez-Osorio, J. G. Lozano, L. Jin, J. W. Somerville, L. C. Duda, A. Nag, A. Walters, K. J. Zhou, *et al.*, Superstructure control of first-cycle voltage hysteresis in oxygen-redox cathodes, *Nature* **577**, 502 (2020).
- [20] E. Boivin, R. A. House, M. A. Pérez-Osorio, J.-J. Marie, U. Maitra, G. J. Rees, and P. G. Bruce, Bulk O<sub>2</sub> formation and Mg displacement explain O-redox in Na<sub>0.67</sub>Mn<sub>0.72</sub>Mg<sub>0.28</sub>O<sub>2</sub>, *Joule* **5**, 1267 (2021).
- [21] R. A. House, H. Y. Playford, R. I. Smith, J. Holter, I. Griffiths, K.-J. Zhou, and P. G. Bruce, Detection of trapped molecular O<sub>2</sub> in a charged Li-rich cathode by neutron PDF, *Energy Environ. Sci.* (2022).
- [22] A. Grenier, G. E. Kamm, Y. Li, H. Chung, Y. S. Meng, and K. W. Chapman, Nanostructure transformation as a signature of oxygen redox in Li-rich 3d and 4d cathodes, *J. Am. Chem. Soc.* **143**, 5763 (2021).
- [23] M. Zhang, D. A. Kitchaev, Z. Lebens-Higgins, J. Vinckeviciute, M. Zuba, P. J. Reeves, C. P. Grey, M. S. Whittingham, L. F. J. Piper, A. Van der Ven, and Y. S. Meng, Pushing the limit of 3d transition metal-based layered oxides that use both cation and anion redox for energy storage, *Nat. Rev. Mater.* **7**, 522 (2022).
- [24] J. M. Tarascon, G. Vaughan, Y. Chabre, L. Seguin, M. Anne, P. Strobel, and G. Amatucci, *In situ* structural and electrochemical study of Ni<sub>1-x</sub>Co<sub>x</sub>O<sub>2</sub> metastable oxides prepared by soft chemistry, *J. Solid State Chem.* **147**, 410 (1999).
- [25] L. Croguennec, C. Pouillerie, A. N. Mansour, and C. Delmas, Structural characterisation of the highly deintercalated Li<sub>x</sub>Ni<sub>1.02</sub>O<sub>2</sub> phases (with x ≤ 0.30), *J. Mater. Chem.* **11**, 131 (2001).
- [26] Y. W. Tsai, B. J. Hwang, G. Ceder, H. S. Sheu, D. G. Liu, and J. F. Lee, *In-situ* x-ray absorption spectroscopic study on variation of electronic transitions and local structure of LiNi<sub>1/3</sub>Co<sub>1/3</sub>Mn<sub>1/3</sub>O<sub>2</sub> cathode material during electrochemical cycling, *Chem. Mater.* **17**, 3191 (2005).
- [27] J.-N. Zhang, Q. Li, C. Ouyang, X. Yu, M. Ge, X. Huang, E. Hu, C. Ma, S. Li, R. Xiao, *et al.*, Trace doping of multiple elements enables stable battery cycling of LiCoC<sub>2</sub> at 4.6 V, *Nat. Energy* **4**, 594 (2019).
- [28] W. Kong, D. Wong, K. An, J. Zhang, Z. Chen, C. Schulz, Z. Xu, and X. Liu, Stabilizing the anionic redox in 4.6 V LiCoO<sub>2</sub> cathode through adjusting oxygen magnetic moment, *Adv. Funct. Mater.* **32**, 2202679 (2022).
- [29] E. Hu, Q. Li, X. Wang, F. Meng, J. Liu, J.-N. Zhang, K. Page, W. Xu, L. Gu, R. Xiao, *et al.*, Oxygen-redox reactions in LiCoO<sub>2</sub> cathode without O–O bonding during charge-discharge, *Joule* **5**, 720 (2021).
- [30] K.-Y. Park, Y. Zhu, C. G. Torres-Castanedo, H. J. Jung, N. S. Luu, O. Kahvecioglu, Y. Yoo, J.-W. T. Seo, J. R. Downing, H.-D. Lim, *et al.*, Elucidating and mitigating high-voltage degradation cascades in cobalt-free LiNiO<sub>2</sub> lithium-ion battery cathodes, *Adv. Mater.* **34**, 2106402 (2022).
- [31] G.-H. Lee, J. Wu, D. Kim, K. Cho, M. Cho, W. Yang, and Y.-M. Kang, Reversible anionic redox activities in conventional LiNi<sub>1/3</sub>Co<sub>1/3</sub>Mn<sub>1/3</sub>O<sub>2</sub> cathodes, *Angew. Chem., Int. Ed.* **59**, 8681 (2020).
- [32] X. Liu, *et al.*, Origin and regulation of oxygen redox instability in high-voltage battery cathodes, *Nature Energy* **7**, 808 (2022).
- [33] S. Li, Z. Liu, L. Yang, X. Shen, Q. Liu, Z. Hu, Q. Kong, J. Ma, J. Li, H.-J. Lin, *et al.*, Anionic redox reaction and structural evolution of Ni-rich layered oxide cathode material, *Nano Energy* **98**, 107335 (2022).
- [34] Z. W. Lebens-Higgins, *et al.*, Revisiting the charge compensation mechanisms in LiNi<sub>0.8</sub>Co<sub>0.2-y</sub>Al<sub>y</sub>O<sub>2</sub> systems, *Mater. Horiz.* **6**, 2112 (2019).
- [35] R. Qiao, *et al.*, High-efficiency *in situ* resonant inelastic x-ray scattering (iRIXS) endstation at the advanced light source, *Rev. Sci. Instrum.* **88**, 033106 (2017).
- [36] W. E. Gent, *et al.*, Coupling between oxygen redox and cation migration explains unusual electrochemistry

- in lithium-rich layered oxides, *Nat. Commun.* **8**, 2091 (2017).
- [37] M. J. Zuba, A. Grenier, Z. Lebens-Higgins, G. J. P. Fajardo, Y. Li, Y. Ha, H. Zhou, M. S. Whittingham, W. Yang, Y. S. Meng, *et al.*, Whither Mn oxidation in Mn-rich alkali-excess cathodes?, *ACS Energy Lett.* **6**, 1055 (2021).
- [38] E. Zhao, M. Zhang, X. Wang, E. Hu, J. Liu, X. Yu, M. Olguin, T. A. Wynn, Y. S. Meng, K. Page, *et al.*, Local structure adaptability through multi cations for oxygen redox accommodation in Li-rich layered oxides, *Energy Storage Mater.* **24**, 384 (2020).
- [39] J. Xu, M. Sun, R. Qiao, S. E. Renfrew, L. Ma, T. Wu, S. Hwang, D. Nordlund, D. Su, K. Amine, *et al.*, Elucidating anionic oxygen activity in lithium-rich layered oxides, *Nat. Commun.* **9**, 947 (2018).
- [40] K. Dai, *et al.*, High reversibility of lattice oxygen redox quantified by direct bulk probes of both anionic and cationic redox reactions, *Joule* **3**, 518 (2019).
- [41] J. Wu, Z. Zhuo, X. Rong, K. Dai, Z. Lebens-Higgins, S. Sallis, F. Pan, L. F. J. Piper, G. Liu, Y.-d. Chuang, *et al.*, Dissociate lattice oxygen redox reactions from capacity and voltage drops of battery electrodes, *Sci. Adv.* **6**, eaaw3871 (2020).
- [42] U. Maitra, *et al.*, Oxygen redox chemistry without excess alkali-metal ions in  $\text{Na}_{2/3}[\text{Mg}_{0.28}\text{Mn}_{0.72}]\text{O}_2$ , *Nat. Chem.* **10**, 288 (2018).
- [43] Z. Zhuo, Y.-s. Liu, J. Guo, Y.-d. Chuang, F. Pan, and W. Yang, Full energy range resonant inelastic x-ray scattering of  $\text{O}_2$  and  $\text{CO}_2$ : Direct comparison with oxygen redox state in batteries, *J. Phys. Chem. Lett.* **11**, 2618 (2020).
- [44] J. Wu, Q. Li, S. Sallis, Z. Zhuo, W. E. Gent, W. C. Chueh, S. Yan, Y.-d. Chuang, and W. Yang, Fingerprint oxygen redox reactions in batteries through high-efficiency mapping of resonant inelastic x-ray scattering, *Condens. Matter* **4**, 5 (2019).
- [45] J. Zheng, Y. Ye, T. Liu, Y. Xiao, C. Wang, F. Wang, and F. Pan, Ni/Li Disordering in layered transition metal oxide: Electrochemical impact, origin, and control, *Acc. Chem. Res.* **52**, 2201 (2019).
- [46] H.-H. Ryu, G.-T. Park, C. S. Yoon, and Y.-K. Sun, Suppressing detrimental phase transitions via tungsten doping of  $\text{LiNiO}_2$  cathode for next-generation lithium-ion batteries, *J. Mater. Chem. A* **7**, 18580 (2019).
- [47] D. Rathore, C. Geng, N. Zaker, I. Hamam, Y. Liu, P. Xiao, G. A. Botton, J. Dahn, and C. Yang, Tungsten infused grain boundaries enabling universal performance enhancement of Co-free Ni-rich cathode materials, *J. Electrochem. Soc.* **168**, 120514 (2021).
- [48] C. Geng, D. Rathore, D. Heino, N. Zhang, I. Hamam, N. Zaker, G. A. Botton, R. Omessi, N. Phattharasupakun, T. Bond, *et al.*, Mechanism of action of the tungsten dopant in  $\text{LiNiO}_2$  positive electrode materials, *Adv. Energy Mater.* **12**, 2103067 (2022).
- [49] D. Goonetilleke, A. Mazilkin, D. Weber, Y. Ma, F. Fauth, J. Janek, T. Brezesinski, and M. Bianchini, Single step synthesis of W-modified  $\text{LiNiO}_2$  using an ammonium tungstate flux, *J. Mater. Chem. A* **10**, 7841 (2022).
- [50] M. D. Radin, J. Vinckeviciute, R. Seshadri, and A. Van der Ven, Manganese oxidation as the origin of the anomalous capacity of Mn-containing Li-excess cathode materials, *Nat. Energy* **4**, 639 (2019).
- [51] H. Hafiz, K. Suzuki, B. Barbiellini, N. Tsuji, N. Yabuuchi, K. Yamamoto, Y. Orikasa, Y. Uchimoto, Y. Sakurai, H. Sakurai, *et al.*, Tomographic reconstruction of oxygen orbitals in lithium-rich battery materials, *Nature* **594**, 213 (2021).
- [52] K. Luo, M. R. Roberts, R. Hao, N. Guerrini, D. M. Pickup, Y. S. Liu, K. Edstrom, J. Guo, A. V. Chadwick, L. C. Duda, and P. G. Bruce, Charge-compensation in 3d-transition-metal-oxide intercalation cathodes through the generation of localized electron holes on oxygen, *Nat. Chem.* **8**, 684 (2016).
- [53] K. Luo, M. R. Roberts, N. Guerrini, N. Tapia-Ruiz, R. Hao, F. Massel, D. M. Pickup, S. Ramos, Y. S. Liu, J. Guo, *et al.*, Anion redox chemistry in the cobalt free 3d transition metal oxide intercalation electrode  $\text{Li}[\text{Li}_{0.2}\text{Ni}_{0.2}\text{Mn}_{0.6}]\text{O}_2$ , *J. Am. Chem. Soc.* **138**, 11211 (2016).
- [54] M. Okubo and A. Yamada, Molecular orbital principles of oxygen-redox battery electrodes, *ACS Appl. Mater. Interfaces* **9**, 36463 (2017).
- [55] See the Supplemental Material at <http://link.aps.org/supplemental/10.1103/PRXEnergy.2.013005> for XRD analysis of pristine WLNO, x-ray absorption spectroscopy of WLNO, Pawley analysis of *ex situ* XRD data of cycled electrodes, soft XAS data of WLNO electrodes, hard x-ray photoelectron spectroscopy (HAXPES) data, and high-resolution RIXS data; it also includes Refs. [56–58,64,77, 97–102].
- [56] H. M. Rietveld, Line profiles of neutron powder-diffraction peaks for structure refinement, *Acta Crystallogr.* **22**, 151 (1967).
- [57] H. M. Rietveld, A profile refinement method for nuclear and magnetic structures, *J. Appl. Crystallogr.* **2**, 65 (1969).
- [58] A. Rougier, P. Gravereau, and C. Delmas, Optimization of the composition of the  $\text{Li}_{1-x}\text{Ni}_{1+x}\text{O}_2$  electrode materials: Structural, magnetic, and electrochemical studies, *J. Electrochem. Soc.* **143**, 1168 (1996).
- [59] A. R. Genreith-Schriever, H. Banerjee, A. S. Menon, E. N. Bassey, L. F. Piper, C. P. Grey, A. J. Morris, Oxygen Hole Formation Controls Stability in  $\text{LiNiO}_2$  Cathodes: DFT Studies of Oxygen Loss and Singlet Oxygen Formation in Li-Ion Batteries, arXiv, arXiv:2205.10462v2 (2022).
- [60] J. Xu, E. Hu, D. Nordlund, A. Mehta, S. N. Ehrlich, X.-Q. Yang, and W. Tong, Understanding the degradation mechanism of lithium nickel oxide cathodes for Li-ion batteries, *ACS Appl. Mater. Interfaces* **8**, 31677 (2016).
- [61] R. Qiao, L. A. Wray, J.-H. Kim, N. P. W. Pieczonka, S. J. Harris, and W. Yang, Direct experimental probe of the  $\text{Ni}(\text{II})/\text{Ni}(\text{III})/\text{Ni}(\text{IV})$  redox evolution in  $\text{LiNi}_{0.5}\text{Mn}_{1.5}\text{O}_4$  electrodes, *J. Phys. Chem. C* **119**, 27228 (2015).
- [62] C. S. Yoon, M.-J. Choi, D.-W. Jun, Q. Zhang, P. Kagazchi, K.-H. Kim, and Y.-K. Sun, Cation ordering of Zr-doped  $\text{LiNiO}_2$  cathode for lithium-ion batteries, *Chem. Mater.* **30**, 1808 (2018).
- [63] W. E. O'Grady, K. I. Pandya, K. E. Swider, and D. A. Corrigan, *In situ* x-ray absorption near-edge structure evidence for quadrivalent nickel in nickel battery electrodes, *J. Electrochem. Soc.* **143**, 1613 (1996).

- [64] H. Li, N. Zhang, J. Li, and J. R. Dahn, Updating the structure and electrochemistry of  $\text{Li}_x\text{NiO}_2$  for  $0 \leq x \leq 1$ , *J. Electrochem. Soc.* **165**, A2985 (2018).
- [65] L. de Biasi, A. Schiele, M. Roca-Ayats, G. Garcia, T. Brezesinski, P. Hartmann, and J. Janek, Phase transformation behavior and stability of  $\text{LiNiO}_2$  cathode material for Li-ion batteries obtained from *in situ* gas analysis and *operando* x-ray diffraction, *ChemSusChem* **12**, 2240 (2019).
- [66] C. Xu, P. J. Reeves, Q. Jacquet, and C. P. Grey, Phase behavior during electrochemical cycling of Ni-rich cathode materials for Li-ion batteries, *Adv. Energy Mater.* **11**, 2003404 (2021).
- [67] L. Croguennec, C. Pouillerie, and C. Delmas, Structural characterisation of new metastable  $\text{NiO}_2$  phases, *Solid State Ionics* **135**, 259 (2000).
- [68] H. Arai, M. Tsuda, K. Saito, M. Hayashi, K. Takei, and Y. Sakurai, Structural and thermal characteristics of nickel dioxide derived from  $\text{LiNiO}_2$ , *J. Solid State Chem.* **163**, 340 (2002).
- [69] N. Ikeda, I. Konuma, H. B. Rajendra, T. Aida, and N. Yabuuchi, Why is the O<sub>3</sub> to O<sub>1</sub> phase transition hindered in  $\text{LiNiO}_2$  on full delithiation?, *J. Mater. Chem. A* **9**, 15963 (2021).
- [70] M. E. Arroyo y de Dompablo, A. Van der Ven, and G. Ceder, First-principles calculations of lithium ordering and phase stability on  $\text{LiNiO}_2$ , *Phys. Rev. B* **66**, 064112 (2002).
- [71] C. Wang, R. Zhang, K. Kisslinger, and H. L. Xin, Atomic-scale observation of O<sub>1</sub> faulted phase-induced deactivation of  $\text{LiNiO}_2$  at high voltage, *Nano Lett.* **21**, 3657 (2021).
- [72] C. Wang, L. Han, R. Zhang, H. Cheng, L. Mu, K. Kisslinger, P. Zou, Y. Ren, P. Cao, F. Lin, and H. L. Xin, Resolving atomic-scale phase transformation and oxygen loss mechanism in ultrahigh-nickel layered cathodes for cobalt-free lithium-ion batteries, *Matter* **4**, 2013 (2021).
- [73] C. Delmas, C. Fouassier, and P. Hagenmuller, Structural classification and properties of the layered oxides, *Physica B+C* **99**, 81 (1980).
- [74] J. Bréger, Y. S. Meng, Y. Hinuma, S. Kumar, K. Kang, Y. Shao-Horn, G. Ceder, and C. P. Grey, Effect of high voltage on the structure and electrochemistry of  $\text{LiNi}_{0.5}\text{Mn}_{0.5}\text{O}_2$ : A joint experimental and theoretical study, *Chem. Mater.* **18**, 4768 (2006).
- [75] A. N. Mansour, X. Q. Yang, X. Sun, J. McBreen, L. Croguennec, and C. Delmas, *In situ* x-ray absorption spectroscopy study of  $\text{Li}_{1-z}\text{Ni}_{1+z}\text{O}_2$  ( $z \leq 0.02$ ) cathode material, *J. Electrochem. Soc.* **147**, 2104 (2000).
- [76] J. Xu, F. Lin, D. Nordlund, E. J. Crumlin, F. Wang, J. Bai, M. M. Doeff, and W. Tong, Elucidation of the surface characteristics and electrochemistry of high-performance  $\text{LiNiO}_2$ , *Chem. Commun.* **52**, 4239 (2016).
- [77] M. Bianchini, A. Schiele, S. Schweidler, S. Siculo, F. Fauth, E. Suard, S. Indris, A. Mazilkin, P. Nagel, S. Schuppler, *et al.*, From  $\text{LiNiO}_2$  to  $\text{Li}_2\text{NiO}_3$ : Synthesis, structures and electrochemical mechanisms in Li-rich nickel oxides, *Chem. Mater.* **32**, 9211 (2020).
- [78] A. Weber and E. A. McGinnis, The Raman spectrum of gaseous oxygen, *J. Mol. Spectrosc.* **4**, 195 (1960).
- [79] M. Ben Yahia, J. Vergnet, M. Saubanere, and M. L. Doublet, Unified picture of anionic redox in Li/Na-Ion Batteries, *Nat. Mater.* **18**, 496 (2019).
- [80] W. E. Gent, I. I. Abate, W. Yang, L. F. Nazar, and W. C. Chueh, Design rules for high-valent redox in intercalation electrodes, *Joule* **4**, 1369 (2020).
- [81] T. Sudayama, K. Uehara, T. Mukai, D. Asakura, X.-M. Shi, A. Tsuchimoto, B. Mortemard de Boisse, T. Shimada, E. Watanabe, Y. Harada, *et al.*, Multiorbital bond formation for stable oxygen-redox reaction in battery electrodes, *Energy Environ. Sci.* **13**, 1492 (2020).
- [82] P. Whitfield, I. Davidson, L. Cranswick, I. Swainson, and P. Stephens, Investigation of possible superstructure and cation disorder in the lithium battery cathode material  $\text{LiMn}_{1/3}\text{Ni}_{1/3}\text{Co}_{1/3}\text{O}_2$  using neutron and anomalous dispersion powder diffraction, *Solid State Ionics* **176**, 463 (2005).
- [83] L. Yin, Z. Li, G. S. Mattei, J. Zheng, W. Zhao, F. Omenya, C. Fang, W. Li, J. Li, Q. Xie, *et al.*, Thermodynamics of antisite defects in layered NMC cathodes: Systematic insights from high-precision powder diffraction analyses, *Chem. Mater.* **32**, 1002 (2019).
- [84] J. Liu, Z. Du, X. Wang, S. Tan, X. Wu, L. Geng, B. Song, P.-H. Chien, S. M. Everett, and E. Hu, Anionic redox induced anomalous structural transition in Ni-rich cathodes, *Energy Environ. Sci.* **14**, 6441 (2021).
- [85] P. Kurzhals, F. Riewald, M. Bianchini, H. Sommer, H. A. Gasteiger, and J. Janek, The  $\text{LiNiO}_2$  cathode active material: A comprehensive study of calcination conditions and their correlation with physicochemical properties. Part I. Structural chemistry, *J. Electrochem. Soc.* **168**, 110518 (2021).
- [86] C. Xu, K. Märker, J. Lee, A. Mahadevegowda, P. J. Reeves, S. J. Day, M. F. Groh, S. P. Emge, C. Ducati, B. Layla Mehdi, *et al.*, Bulk fatigue induced by surface reconstruction in layered Ni-rich cathodes for Li-ion batteries, *Nat. Mater.* **20**, 84 (2021).
- [87] J. Rana, J. K. Papp, Z. Lebens-Higgins, M. Zuba, L. A. Kaufman, A. Goel, R. Schmuck, M. Winter, M. S. Whittingham, W. Yang, *et al.*, Quantifying the capacity contributions during activation of  $\text{Li}_2\text{MnO}_3$ , *ACS Energy Lett.* **5**, 634 (2020).
- [88] H. Li, A. J. Perez, B. Taudul, T. D. Boyko, J. W. Freeland, M.-L. Doublet, J.-M. Tarascon, and J. Cabana, Elucidation of active oxygen sites upon delithiation of  $\text{Li}_3\text{IrO}_4$ , *ACS Energy Lett.* **6**, 140 (2021).
- [89] P.-H. Chien, X. Wu, B. Song, Z. Yang, C. K. Waters, M. S. Everett, F. Lin, Z. Du, and J. Liu, New insights into structural evolution of  $\text{LiNiO}_2$  revealed by *operando* neutron diffraction, *Batteries Supercaps* **4**, 1701 (2021).
- [90] Y. Takeda, R. Kanno, M. Sakano, O. Yamamoto, M. Takano, Y. Bando, H. Akinaga, K. Takita, and J. B. Goodenough, Crystal chemistry and physical properties of  $\text{La}_{2-x}\text{Sr}_x\text{NiO}_4$  ( $0 \leq x \leq 1.6$ ), *Mater. Res. Bull.* **25**, 293 (1990).
- [91] T. Kamiyana, F. Izumi, H. Asano, H. Takagi, S. Uchida, Y. Tokurs, E. Takayama-Muromachi, M. Matsuda, Y. Endoh, and Y. Hidaka, Sr-induced oxygen defects in  $\text{La}_{2-x}\text{Sr}_x\text{CuO}_{4-\delta}$  a neutron powder diffraction study, *Phys. C* **172**, 120 (1990).

- [92] F. Lechermann, W. Körner, D. F. Urban, and C. Elsässer, Interplay of charge-transfer and Mott-Hubbard physics approached by an efficient combination of self-interaction correction and dynamical mean-field theory, *Phys. Rev. B* **100**, 115125 (2019).
- [93] J. Y. Zhang, W. W. Li, R. L. Z. Hoye, J. L. MacManus-Driscoll, M. Budde, O. Bierwagen, L. Wang, Y. Du, M. J. Wahila, L. F. J. Piper, *et al.*, Electronic and transport properties of Li-doped NiO epitaxial thin films, *J. Mater. Chem. C* **6**, 2275 (2018).
- [94] T. Mizokawa, Y. Wakisaka, T. Sudayama, C. Iwai, K. Miyoshi, J. Takeuchi, H. Wadati, D. G. Hawthorn, T. Z. Regier, and G. A. Sawatzky, Role of Oxygen Holes in  $\text{Li}_x\text{CoO}_2$  Revealed by Soft X-Ray Spectroscopy, *Phys. Rev. Lett.* **111**, 056404 (2013).
- [95] J. M. Tranquada, John Goodenough and the many lives of transition-metal oxides, *J. Electrochem. Soc.* **169**, 010535 (2022).
- [96] G. Assat and J.-M. Tarascon, Fundamental understanding and practical challenges of anionic redox activity in Li-ion batteries, *Nat. Energy* **3**, 373 (2018).
- [97] G. S. Pawley, Unit-cell refinement from powder diffraction scans, *J. Appl. Crystallogr.* **14**, 357 (1981).
- [98] A. A. Coelho, TOPAS and TOPAS-Academic: An optimization program integrating computer algebra and crystallographic objects written in C++, *J. Appl. Crystallogr.* **51**, 210 (2018).
- [99] E. P. Jahrman, W. M. Holden, A. S. Ditter, D. R. Mortensen, G. T. Seidler, T. T. Fister, S. A. Kozimor, L. F. J. Piper, J. Rana, N. C. Hyatt, and M. C. Stennett, An improved laboratory-based x-ray absorption fine structure and x-ray emission spectrometer for analytical applications in materials chemistry research, *Rev. Sci. Instrum.* **90**, 024106 (2019).
- [100] B. Ravel and M. Newville, Athena, Artemis, Hephaestus: Data analysis for x-ray absorption spectroscopy using IFEFFIT, *J. Synchrotron Radiat.* **12**, 537 (2005).
- [101] K.-J. Zhou, *et al.*, I21: An advanced high-resolution resonant inelastic x-ray scattering beamline at Diamond Light Source, *J. Synchrotron Radiat.* **29**, 563 (2022).
- [102] J. F. Mark Basham, Michael T. Wharmby, Peter C. Y. Chang, Baha El Kassaby, Matthew Gerring, Jun Aishima, Karl Levik, Bill C. A. Pulford, Irakli Sikharulidze, Duncan Sneddon, *et al.*, Data analysis workbench (DAWN), *J. Synchrotron Radiat.* **22**, 853 (2015).